Int. J. Multiphase Flow Vol. 12, No. 3, pp. 389–403, 1986
Printed in Great Britain

0301–9322/86 $3.00+.00
Pergamon Journals/Elsevier

EFFECTS OF DROPLET-SIZE DISTRIBUTION AND GAS-PHASE FLOW SEPARATION UPON INERTIA COLLECTION OF DROPLETS BY BLUFF-BODIES IN GAS–LIQUID MIST FLOW

TOSHIO AIHARA and WU-SHUNG FU
Institute of High Speed Mechanics, Tohoku University, Sendai 980, Japan

(*Received* 11 *March* 1985; *in revised form* 21 *July* 1985)

Abstract—This paper describes a trajectory analysis of the inertia collection of monodisperse- and polydisperse-droplets by a normal flat plate and a circular cylinder in gas–liquid mist flow, taking into account the far-wake displacement effect of gas-phase flow. The effects of the far-upstream droplet-size distribution and the gas-phase flow separation upon the local collection efficiency and the velocities and size distribution of droplets on impingement are examined. On the basis of these results, a new equivalent diameter of polydisperse-droplets is proposed.

1. INTRODUCTION

Cooling of heated bodies by suspending water droplets in a gas stream has a remarkably improved performance of heat transfer in comparison with single-phase gas cooling; accordingly, this gas–water mist cooling is considered to be available for a significant reduction in the size and weight of heat exchangers and for emergency cooling at peak loads or in accident of normally gas-cooled equipment such as nuclear reactors.

The heat transfer of gas–water mist flow is an extremely complicated phenomenon which depends on the size distribution of water droplets in freestream, the droplet trajectories, and the flow behavior and evaporation of water film on a heated body, etc. Consequently, although many theoretical and experimental studies have been made, the majority of existing theoretical studies are focused on either the heat transfer from dry surface or the flow behavior and evaporation of water film, without consideration for the droplet trajectories; for instance, Hodgson & Sunderland (1968), Thomas & Sunderland (1970), Aihara *et al.* (1979), Nishikawa & Takase (1979), and Aihara & Fu (1982). The droplet trajectories are taken into consideration only by Goldstein *et al.* (1967) and Lu & Heyt (1980).

As for the droplet trajectory and collection efficiency, with no heat transfer, many analyses have hitherto been made by using various models: in the case of a circular cylinder or a sphere, an unseparated potential flow model has been adopted as gas-phase streamlines, (e.g. Healy 1970; Morsi & Alexander 1972). In the case of a normal flat plate, Hess's free-streamline theory (1973), which gives a wake flow rather different from the real wake bubble, is used to calculate the gas-phase streamlines (e.g. Ushiki *et al.* 1977).

In this paper the inviscid bluff-body wake model by Kiya & Arie (1977), including far-wake displacement effect, is used to make a trajectory analysis of the local impinging velocities and partial collection efficiency of monodisperse-droplets by a normal flat plate and a circular cylinder, immersed in a gas–liquid mist flow. Furthermore in the case of polydisperse-droplets, the effects are examined of the size-distribution of droplets in freestream upon the impingement size-distribution and total collection efficiency; and then a new equivalent diameter is proposed.

2. CASE OF MONODISPERSE-DROPLETS

2.1 *Physical model and governing equations*

We consider a flat plate or a circular cylinder of a characteristic dimension l immersed in a crossflow of gas–liquid mist with velocity $u_{G\infty}$, as shown in figure 1. Suppose that a droplet, being far-upstream at a distance y_0 from the axis of symmetry, impinges at a

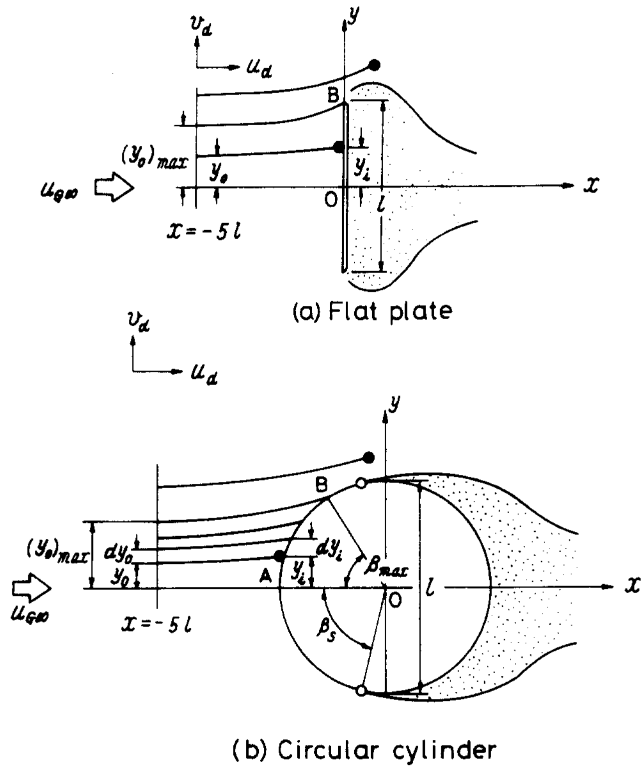

Figure 1. Physical model.

distance y_i onto the body. Let $(y_0)_{max}$ be the far-upstream position of the droplet which just grazes the body. In the case of a plate, the grazing points B coincide with the separation points; however, in the case of a cylinder, the grazing points B do not always coincide with the separation points, shown by angle β_s in figure 1(b).

The following, some of which are discussed in appendix A, are assumed for simplification.

(1) The gas flow is steady, two-dimensional and laminar.
(2) The thickness of the gas-phase boundary layer is very small, compared with the characteristic dimension l.
(3) The liquid droplets are spherical, rigid particles of a diameter d_d and are uniformly distributed in the gas-phase far-upstream.
(4) The cloud of droplets at a low concentration does not affect the gas-phase flow pattern; and the droplet–droplet interaction is negligible.
(5) The gas–droplet interaction follows the drag law for a single rigid particle.
(6) The droplets have the same velocity as the gas-phase at a distance $5l$ upstream of the body.
(7) All physical properties remain constant.
(8) The influence of gravity, electrostatic force, free-stream turbulence and the Saffman effect are negligible.

Subject to these assumptions, the equations of motion of a small droplet are

$$m_d \frac{\mathrm{d}u_d}{\mathrm{d}t} = \frac{1}{2} C_D \rho_G A_d |\mathbf{w}_r| (u_G - u_d) \quad , \qquad [1]$$

$$m_d \frac{\mathrm{d}v_d}{\mathrm{d}t} = \frac{1}{2} C_D \rho_G A_d |\mathbf{w}_r| (v_G - v_d) \quad , \qquad [2]$$

and the initial conditions are

$$\text{at } x/l = -5 \quad , \qquad u_d = u_G \qquad \text{and} \qquad v_d = v_G \quad . \qquad [3]$$

Here, m_d and A_d are the mass and projected area of the droplet; ρ_G the gas density; t the time; C_D the drag coefficient; u_d and v_d the droplet velocities in x- and y-directions (as shown in figure 1); $\mathbf{w}_r$ the relative velocity vector between the gas-phase and the droplet; u_G and v_G the gas-velocity components, which are evaluated on the basis of Kiya & Arie's theory (1977), using an inviscid bluff-body wake model, allowing for the far-wake displacement effect.

2.2 Summary of numerical method

Introducing the dimensionless variables

$$\begin{aligned} &X = x/l \ , \quad Y = y/l \ , \quad U_d = u_d/u_{G\infty} \ , \quad V_d = v_d/u_{G\infty} \ , \\ &U_G = u_G/u_{G\infty} \ , \quad V_G = v_G/u_{G\infty} \ , \quad |\mathbf{W}_r| = |\mathbf{w}_r|/u_{G\infty} \ , \quad \tau = t\,u_{G\infty}/l \ , \end{aligned} \qquad [4]$$

into [1] and [2], it produces the following equations:

$$K\frac{\mathrm{d}U_d}{\mathrm{d}\tau} = \frac{C_D\mathrm{Re}_d}{24}|\mathbf{W}_r|(U_G - U_d) \ , \qquad [5]$$

$$K\frac{\mathrm{d}V_d}{\mathrm{d}\tau} = \frac{C_D\mathrm{Re}_d}{24}|\mathbf{W}_r|(V_G - V_d) \qquad [6]$$

with

$$K = \frac{1}{18}\left(\frac{d_d}{l}\right)\left(\frac{\rho_d}{\rho_G}\right)\mathrm{Re}_d \ . \qquad [7]$$

Here K is called the inertia parameter, ρ_d the liquid density, and Re_d the droplet freestream Reynolds number, defined by:

$$\mathrm{Re}_d = d_d\,u_{G\infty}/\nu_G \qquad [8]$$

where ν_G is the kinematic viscosity of gas. As for the droplet drag coefficient C_D, Morsi & Alexander's (1972) polynomial approximation is used as

$$C_D = C_0 + \frac{C_1}{\mathrm{Re}_d|\mathbf{W}_r|} + \frac{C_2}{\mathrm{Re}_d^2|\mathbf{W}_r|^2} \qquad [9]$$

where C_0, C_1, C_2 are the constants, as given in table 1.

The above dimensionless equations are solved numerically by a forward-marching scheme employing the following finite-difference approximations. This scheme is substantially the same as in the authors' previous report (Aihara & Fu, 1982):

$$U_{d,k+1}^{(n)} = U_{d,k} + \frac{\Delta\tau}{24K}\left[C_0\mathrm{Re}_d|\mathbf{W}_r^{(n-1)}| + C_1 + \frac{C_2}{\mathrm{Re}_d|\mathbf{W}_r^{(n-1)}|}\right]\{U_{G,k+1} - U_{d,k+1}^{(n-1)}\} \ , \qquad [10]$$

$$V_{d,k+1}^{(n)} = V_{d},k + \frac{\Delta\tau}{24K}\left[C_0\mathrm{Re}_d|\mathbf{W}_r^{(n-1)}| + C_1 + \frac{C_2}{\mathrm{Re}_d|\mathbf{W}_r^{(n-1)}|}\right]\{V_{G,k+1} - V_{d,k+1}^{(n-1)}\} \qquad [11]$$

where the superscript (n) refers to the iteration number and the subscripts k and $k+1$ to the values at point (X,Y) and $(X+\Delta X,\ Y+\Delta Y)$, respectively. The dimensionless relative

Table 1. Constants in Morsi & Alexander's approximate equation of the particle drag coefficient C_D

$Re_d\|W_r\|$	C_0	C_1	C_2
< 0.1	0	24	0
0.1–1	3.69	22.73	0.0903
1–10	1.222	29.1667	-3.8889
10–100	0.6167	46.5	-116.67

velocity $|w_r^{(n-1)}|$ is determined by the following equation:

$$|W_r^{(n-1)}| = \left[\left(\frac{U_{G,k} + U_{G,k+1}}{2} - \frac{U_{d,k} + U_{d,k+1}^{(n-1)}}{2}\right)^2 + \left(\frac{V_{G,k} + V_{G,k+1}}{2} - \frac{V_{d,k} + V_{d,k+1}^{(n-1)}}{2}\right)^2\right]^{1/2} . \qquad [12]$$

Using [10] and [11], the droplet velocity components $U_{d,k+1}$ and $V_{d,k+1}$ at a position $(X+\Delta X, Y+\Delta Y)$ are calculated with the iterative procedure, which is repeated until the following criterion for convergence is satisfied:

$$\left|1 - \frac{U_d^{(n)}}{U_d^{(n+1)}}\right| < 10^{-3} \quad , \left|1 - \frac{V_d^{(n)}}{V_d^{(n+1)}}\right| < 10^{-3} \quad . \qquad [13]$$

The sizes of the forward step are determined by

$$\Delta X = U_{d,k+1}\,\Delta\tau \quad , \quad \Delta Y = V_{d,k+1}\,\Delta\tau \quad , \qquad [14]$$

and the starting values of droplet velocity in the iterative procedure are selected, as follows:

$$U_{d,k+1}^{(1)} = U_{d,k} \quad , V_{d,k+1}^{(1)} = V_{d,k} \quad . \qquad [15]$$

As for the time increment $\Delta\tau$, the value decreasing with the advance of droplet is adopted so that the spatial step sizes may be sufficiently fine near the body and that the number of steps for calculating a trajectory may amount to 100–500. The step number less than 90 may produce errors of a few percent or more in numerical results.

The above-mentioned numerical calculation is continued iteratively until the droplet impinges on the body. In the case where the droplet bypasses the body with no collision, the calculation is continued until $X = 3$ or the droplet enters the separated region. The ratio of the mass flow rate of the droplets entering the separated region to that of the droplets collected by the forward portion of a cylinder is described in appendix B.

2.3 Numerical results and discussion

The numerical calculations were made on the air–water mist flow with $\rho_d/\rho_G = 840$, $d_d/l = 3\times10^{-4}$ to 3×10^{-3}, and the gas Reynolds number $Re_G = 1.54\times10^4$, where

$$Re_G = l\,u_{G\infty}/\nu_G \quad . \qquad [16]$$

As for the drag coefficient C_{Db}, base-pressure coefficient C_{pb}, and separation angle β_s of the body which were necessary in applying Kiya & Arie's theory (1977), the same empirical values as in their paper were adopted as follows:

$$C_{Db} = 1.01,\ C_{pb} = -0.96,\ \beta_s = 75° \quad \text{for a circular cylinder,}$$
$$C_{Db} = 2.11,\ C_{pb} = -1.38 \quad \text{for a normal flat plate.}$$

Consequently the variations in the similarity parameters K and Re_d are not independent of each other in the present computations. Two methods are, however, available in reducing the number of these similarity parameters in a practical way. One of them is Langmuir's modified inertia parameter K_0 which is in wide use for presentation of aircraft icing data; its physical meaning is clarified by Bragg (1982), as follows:

$$K_0 = \frac{K}{C_D \mathrm{Re}_d/24} \int_0^1 \frac{d|\mathbf{W}_r|}{|\mathbf{W}_r|} \quad . \tag{17}$$

The other is Bragg's trajectory scaling parameter (1982), $\overline{K}$, expressed as

$$\overline{K} = K/\mathrm{Re}_d^m \quad . \tag{18}$$

Here m is the exponent for which the approximate drag law of $C_D \propto (\mathrm{Re}_d|\mathbf{W}_r|)^{m-1}$ best fits the standard drag curve in the relative velocity range of interest (cf. figures 7 and 8). For convenience, the values of Langmuir's K_0 parameter and Bragg's $\overline{K}$ parameter along with those of m recommended by Bragg, are plotted within the range of the present computations in figure 2.

Figures 3 and 4 show the gas streamlines and droplet trajectories in the vicinity of a plate and a cylinder; it may be seen that the smaller the droplet size d_d/l, the more the droplet is liable to bypass the body.

Figure 5 presents the relations between the starting point y_0 of trajectory-calculation and the impinging point y_i of the droplet onto the body. In the case of a plate, since the grazing trajectory always touches at the edge of the plate regardless of the droplet size (cf. point B in figure 1(a)), all the curves extend to $y_i/l = 0.5$, as shown in figure 5(a). In the case of cylinder, the grazing point shifts downstream with an increase in the droplet size (cf. point B in figure 1(b)); and the y_i/l curves end at the respective grazing points; as shown in figure 5(b). The relations of the starting point for grazing trajectory $(y_0)_{\max}$ vs the relative droplet-size d_d/l are shown in figure 6.

The velocities of droplets on impinging onto the body are plotted in figures 7 and 8. With an increase in droplet diameter, the impinging velocity in x-direction u_{di} increases, but that in y-direction v_{di} decreases; and generally in both cases the velocity components

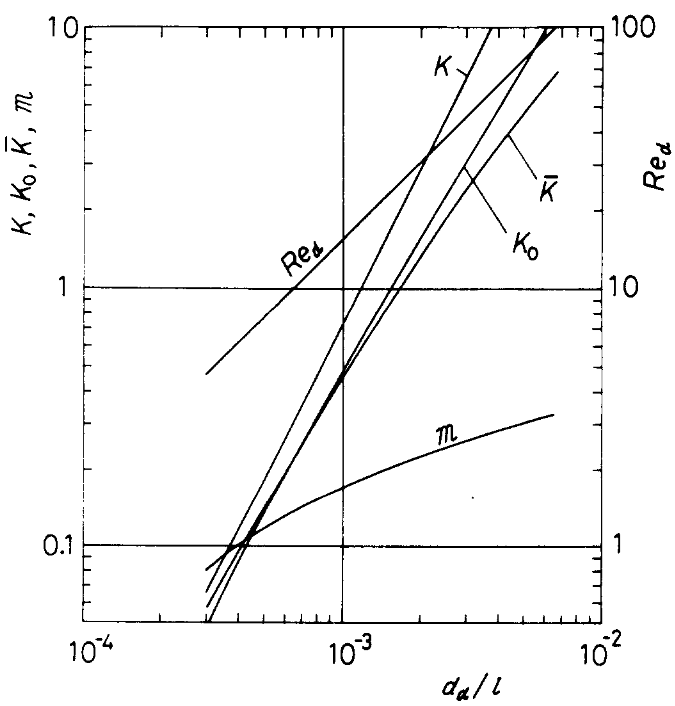

Figure 2. Parameters governing particle trajectories vs d_d/l ($\mathrm{Re}_G = 1.54 \times 10^4$).

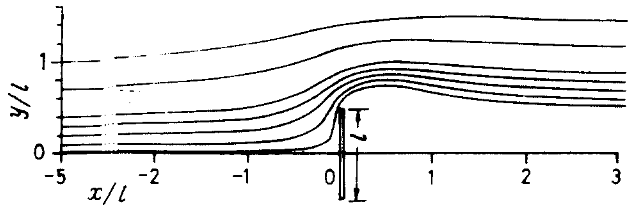

(a) Gas-phase streamlines ($d_d/l = 0$)

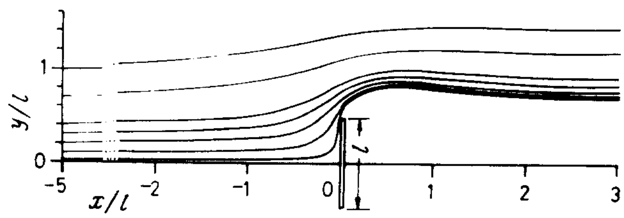

(b) Droplets trajectories ($d_d/l = 3\times10^{-4}$)

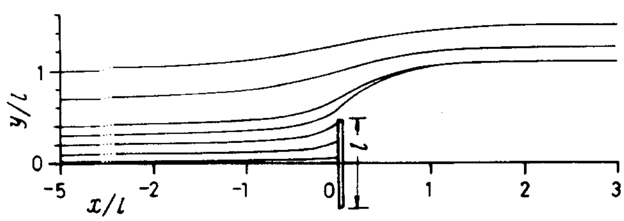

(c) Droplets trajectories ($d_d/l = 10^{-3}$)

Figure 3. Gas streamlines and droplet trajectories near a flat plate.

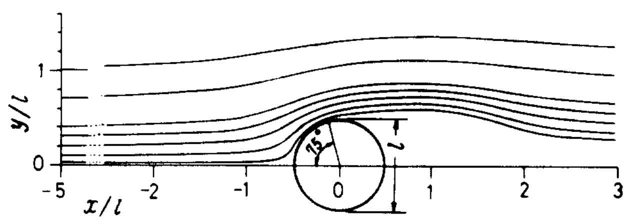

(a) Gas-phase streamlines ($d_d/l = 0$)

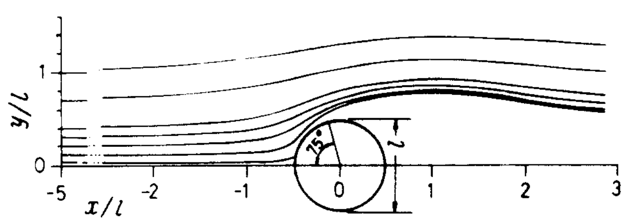

(b) Droplets trajectories ($d_d/l = 5\times10^{-4}$)

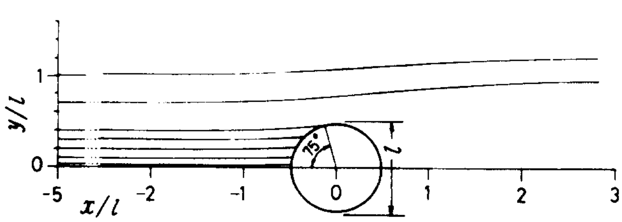

(c) Droplets trajectories ($d_d/l = 3\times10^{-3}$)

Figure 4. Gas streamlines and droplet trajectories near a cylinder.

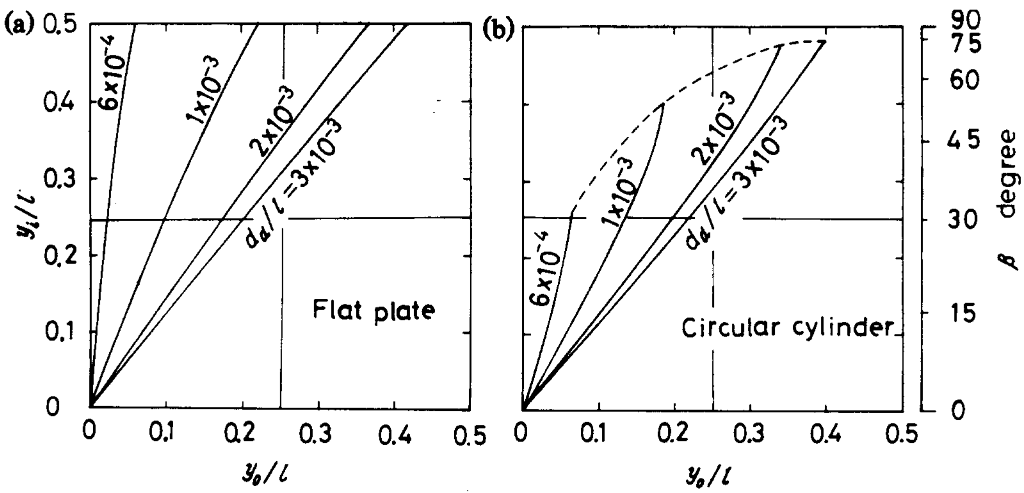

Figure 5. Starting point of calculation y_0 and impinging point of droplet y_i.

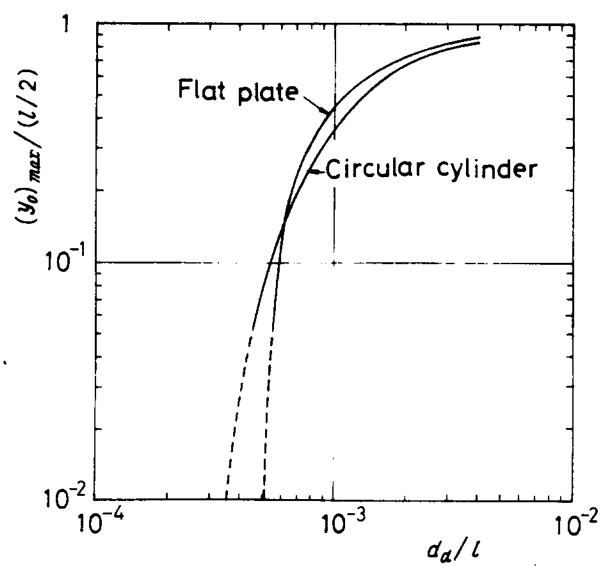

Figure 6. Relations of the starting point $(y_0)_{max}$ of grazing trajectory to the relative droplet-size d_d/l: —— numerically calculated; --- extrapolated.

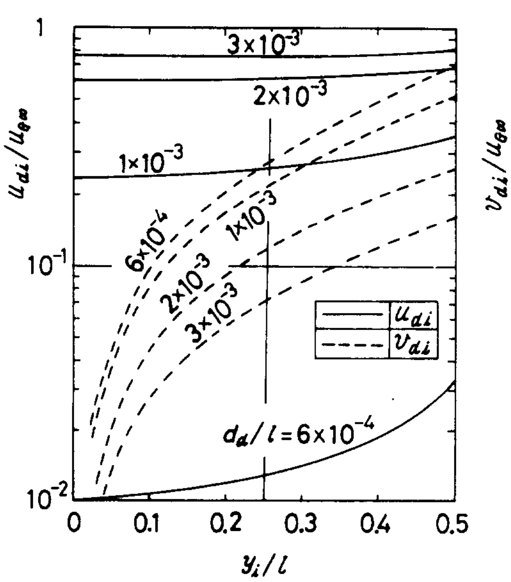

Figure 7. Velocity components u_{di}, v_{di} of droplets impinging onto a normal flat plate.

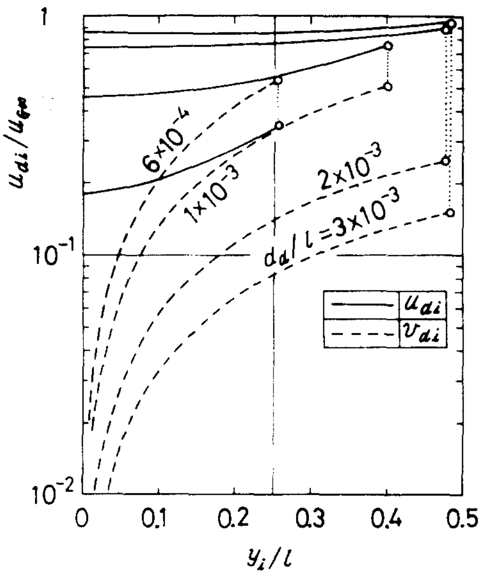

Figure 8. Velocity components u_{di}, v_{di} of droplets impinging onto a circular cylinder. Symbol ○ refers to the grazing point.

increase on being apart from the stagnation point. These arise from the inertia effect of particles, as may be seen from figures 3 and 4.

Figure 9 presents the distributions of the local partial collection efficiency η_c, which is calculated as follows: as may be seen from figure 1(b), the droplets impinging onto an elementary part dy_i on the body are coming through an elementary interval of dy_0 far-upstream. Therefore, if we denote the far-upstream mass flux of droplets by $G_{d\infty}$, the impingement rate is given as $G_{d\infty}dy_0$. Then, the mass flow rate of droplets which will impinge onto the elementary part dy_i, if the streamlines are not diverted by the body, is expressed as $G_{d\infty}dy_i$. Accordingly, the local partial collection efficiency is given as

$$\eta_c = \frac{G_{d\infty}\,dy_0}{G_{d\infty}\,dy_i} = \frac{dy_0}{dy_i}\,. \qquad [19]$$

It is seen by an inspection of figure 9 that the value of η_c for a normal flat plate increases on going away from the stagnation point toward its free edges, though that of a cylinder decreases inversely on approaching toward the grazing point.

In figure 10, the authors' numerical solution is compared with the results of Ushiki *et al.* (1977) in respect to the local partial collection efficiency η_c for a normal flat plate. The

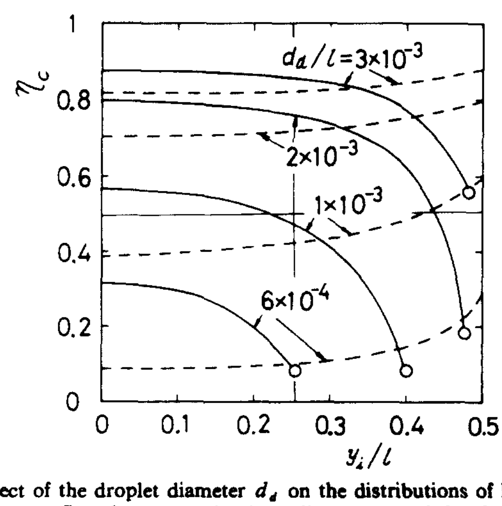

Figure 9. Effect of the droplet diameter d_d on the distributions of local partial collection efficiency η_c: --- flat plate; —— circular cylinder; symbol ○ refers to the grazing point on the cylinder.

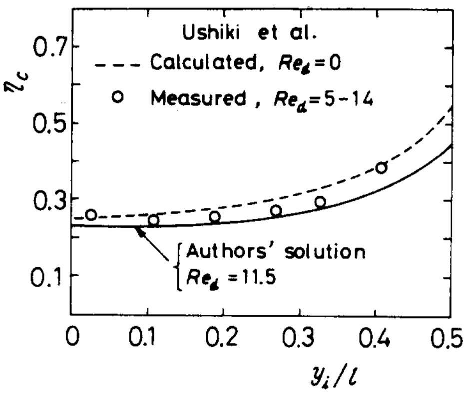

Figure 10. Comparison of the authors' solution with Ushiki *et al.*'s (1977) results in respect of local partial collection efficiency η_c for a normal flat plate ($K \simeq 0.4$).

experimental values of Ushiki *et al.* for a vertical downward flow of air/powder mixture are slightly greater than the authors' solution; and their theoretical values for $\mathrm{Re}_d = 0$, on Hess's discontinuous potential flow (1973), are still greater.

Figure 11 shows differences between the local partial collection efficiencies for a flow with separation and for those without separation. The differences are very large in the case of a flat plate, particularly for small d_d/l; but not in the case of a cylinder.

3. CASE OF POLYDISPERSE-DROPLETS

The reliability of theoretical analysis depends not only upon accuracy in numerical calculation but also on the fidelity of mathematical model for actual phenomenon. Since it is almost impossible in practical applications to obtain monodisperse-droplets, we make an analysis of polydisperse-droplets in this section.

3.1 Physical model and theoretical analysis

First, it is assumed that the polydisperse-droplets of interest have a mass-basis Rosin–Rammler distribution, expressed by [20] and [21], the applicability of which has been experimentally verified by Kudo & Hirata (1978), Aihara *et al.* (1979), Hishida *et al.* (1981) and Aihara *et al.* (1985).

$$R_w = \exp\left[-(d_d/d_c)^n\right] , \qquad [20]$$

$$f_w = -\frac{\mathrm{d}R_w}{\mathrm{d}d_d} = \frac{n}{d_c}\left(\frac{d_d}{d_c}\right)^{n-1} \exp\left[-\left(\frac{d_d}{d_c}\right)^n\right] \qquad [21]$$

where R_w is the cumulative mass fraction contained in drops of diameters greater than d_d, f_w the mass-basis size distribution function, d_c the size parameter and n the dispersion parameter.

Then, according to the definition of $(y_0)_{max}$ in section 2, the impingement rate of the droplets, which are contained in a size interval between d_d and $d_d + \mathrm{d}d_d$, are expressed as

$$G_{d\infty}(y_0)_{max}\, f_w \mathrm{d}d_d \ . \qquad [22]$$

Therefore, the cumulative mass fraction R_w^* of the impinging droplets greater than the size d_d is given by the following equation with a practical accuracy:

$$R_w^* = \frac{\int_{d_d}^{(d_d)_{max}} (y_0)_{max} f_w \mathrm{d}d_d}{\int_{(d_d)_{min}}^{(d_d)_{max}} (y_0)_{max} f_w \mathrm{d}d_d} \ . \qquad [23]$$

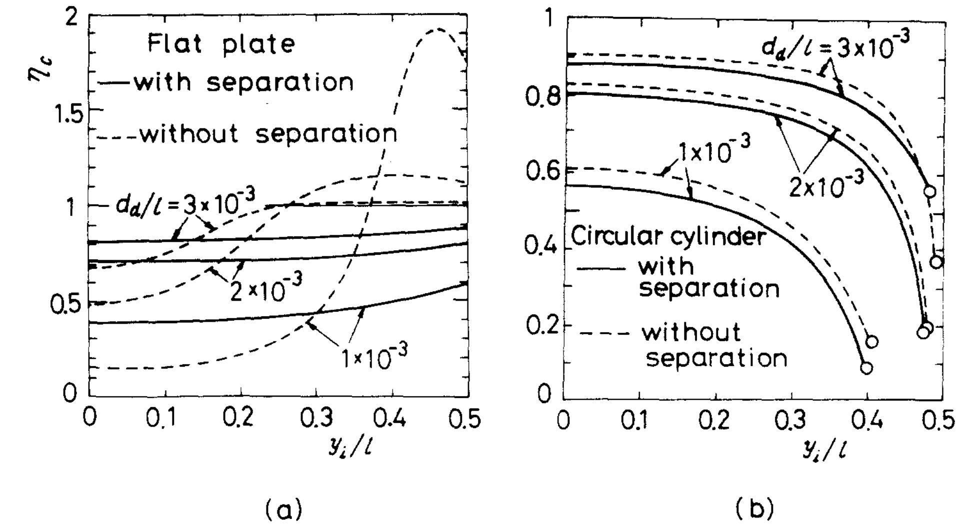

Figure 11. Effect of gas flow separation on local partial collection efficiency η_c.

The numerical integrations of the above equation are carried out with the values of $(y_0)_{max}$ in figure 6 and under the following conditions:

Size intervals,

$$\Delta d_d/l = \begin{cases} 1\times10^{-4} \text{ for } d_d/l \leqq 4\times10^{-3} \ , \\ 2\times10^{-4} \text{ for } d_d/l > 4\times10^{-3} \ , \end{cases} \tag{24}$$

and limits of integration,

$$(d_d)_{max}/l = 8\times10^{-3} \quad \text{and} \quad (d_d)_{min}/l = 1\times10^{-4} \ . \tag{25}$$

3.2 Numerical results and discussion

3.2.1 Droplet size distributions before and after impingement onto the body. The above-mentioned computations are made over the ranges of $d_c/l = 8\times10^{-4}$ to 2×10^{-3} and $n = 1$ to 4. Some of the obtained results are shown in figures 12 and 13, where the size distributions of droplets in freestream are plotted by dashed lines and those of droplets impinging onto the body, by solid curves. The smaller the size parameter d_c, the greater the differences become between the droplet size distributions before and after the impingement. This tendency is more remarkable in a region of smaller droplet size.

3.2.2 Equivalent diameter. Here we propose a new equivalent diameter d_e for practical convenience. This is defined as the diameter of imaginary monodisperse-droplets which would bring about the same rate of total impingement onto the body as the polydisperse-droplets of interest. Hence this equivalent diameter d_e can be obtained by finding the diameter at which the $(y_0)_{max}$-value of monodisperse-droplets, as shown in figure 6, is equal to the value of the denominator in [23] for polydisperse-droplets.

Figure 14 presents the relation between this equivalent diameter d_e and the size parameter d_c. It may be seen that the value of d_e increases with increasing the size and dispersion parameters d_c and n.

Note, the surface mean diameter, or Sauter mean diameter, $\overline{d}_{32}$ and the volume mean diameter, or mass-surface diameter, $\overline{d}_{43}$ may be defined with f_w as follows:

$$\overline{d}_{32} = \frac{\int_{(d_d)_{min}}^{(d_d)_{max}} f_w \, \mathrm{d}d_d}{\int_{(d_d)_{min}}^{(d_d)_{max}} (f_w/d_d) \, \mathrm{d}d_d} \ , \tag{26}$$

$$\overline{d}_{43} = \frac{\int_{(d_d)_{min}}^{(d_d)_{max}} d_d f_w \, \mathrm{d}d_d}{\int_{(d_d)_{min}}^{(d_d)_{max}} f_w \, \mathrm{d}d_d} \ . \tag{27}$$

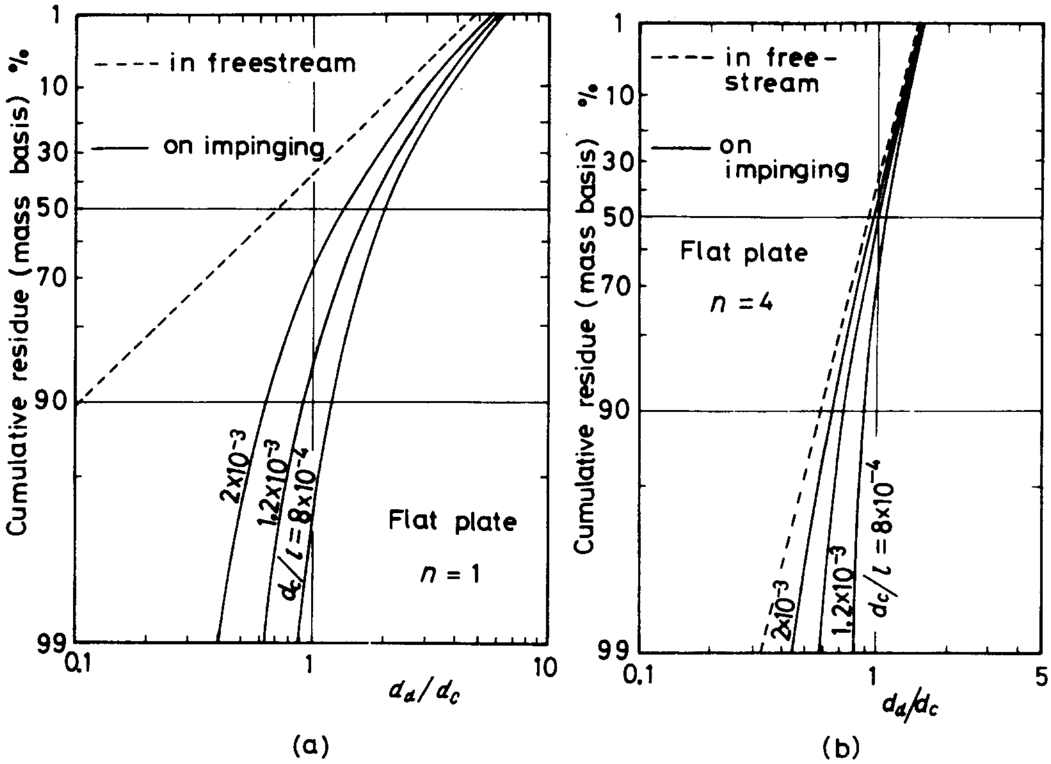

Figure 12. Size distributions of drops in freestream and impinging onto a flat plate.

The values of $\overline{d}_{32}$ and $\overline{d}_{43}$ for droplets in freestream are numerically calculated with the 1-%-diameter as $(d_d)_{min}$ and the 99.9-%-diameter as $(d_d)_{max}$. The obtained results are plotted in the dimensionless form on d_e in figure 15. Here, as the dispersion parameter n is increased, both the surface mean diameter $\overline{d}_{32}$ and volume mean diameter $\overline{d}_{43}$ approach the proposed equivalent diameter d_e, regardless of the shape of body; particularly in the case of $n \geqq 3$, the surface mean diameter $\overline{d}_{32}$ agrees with the equivalent diameter d_e within 10 %.

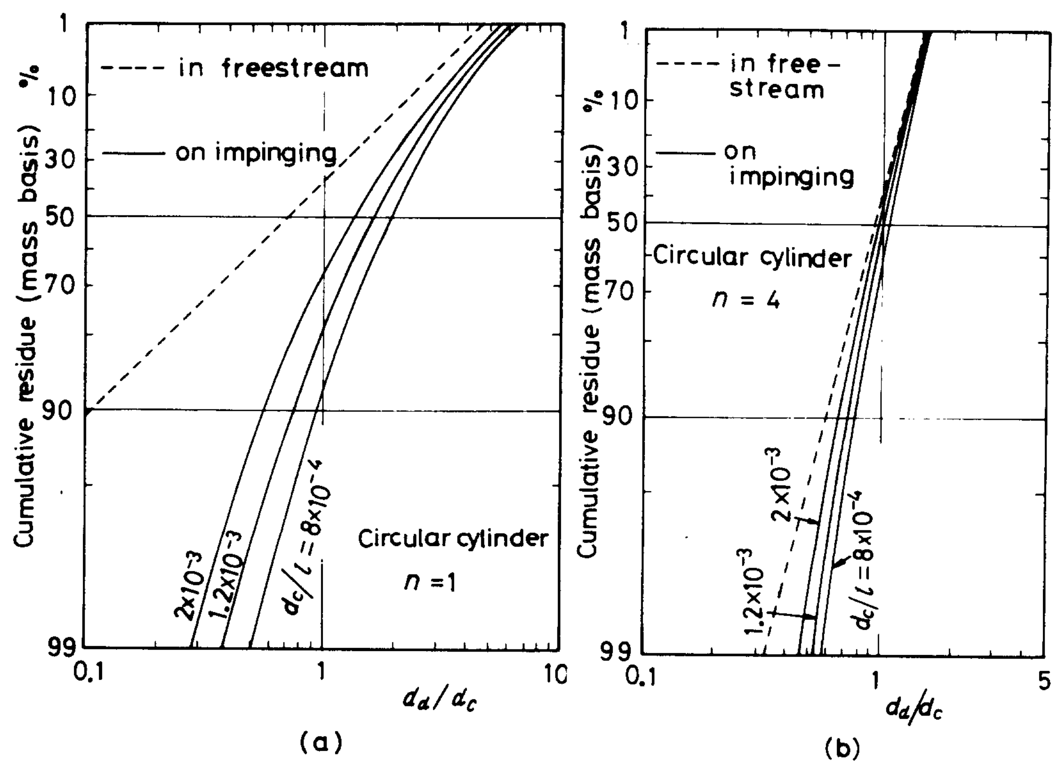

Figure 13. Size distributions of drops in freestream and on impinging onto a circular cylinder.

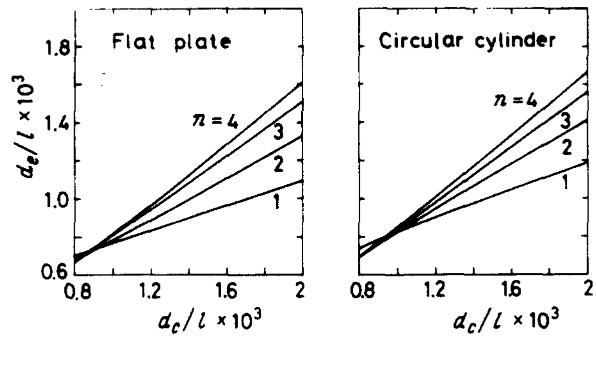

Figure 14. Effect of the droplet size distribution on the proposed equivalent diameter d_e.

Namely, as far as the rate of total droplet-impingement or the total collection efficiency is concerned, it may be recommended that the surface mean diameter $\overline{d}_{32}$, among mean diameters in common use, is the closest to the proposed equivalent diameter.

4. CONCLUSIONS

A trajectory analysis of the inertia collection of monodisperse- and polydisperse-droplets by a flat plate and a circular cylinder in a gas–liquid mist flow has been made by using the inviscid bluff-body wake model which includes far-wake displacement effect. From the numerical results for air–water mist flow, the following conclusions are obtained; their applicability is described in appendix A.

(1) The smaller the droplet, the more the trajectory is liable to bypass the body and to be influenced by the gas flow separation. The smaller the droplet, the nearer the grazing trajectory approaches the flow center line, i.e. stagnation-point streamline. With an increase in droplet diameter, the x-component of the impinging droplet velocity increases and the y-component decreases.

(2) As a general tendency, the larger the droplet, the better becomes the local partial collection efficiency η_c; and the tendency of its distribution depends strongly on the shape of a body. Namely, the η_c of a flat plate increases on approaching toward its free edges, though that of a circular cylinder decreases inversely on approaching its grazing point.

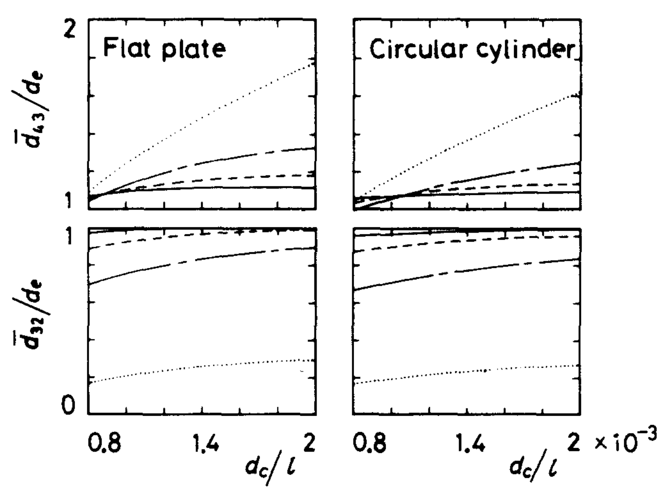

Figure 15. Comparison of the proposed equivalent diameter d_e with the volume mean diameter $\overline{d}_{43}$ and surface mean diameter $\overline{d}_{32}$ in common use. ···· $n=1$; — — — $n=2$; - - - - $n=3$; —— $n=4$.

(3) The effect of the existence of gas flow separation on the local partial collection efficiency is quite prominent for a flat plate, particularly in the case of small droplets, but slight for a circular cylinder.
(4) The smaller the size parameter, the greater the differences become between the size distributions of polydisperse-droplets before and after the impingement onto the body. This tendency is more remarkable in a region of smaller droplet size.
(5) A new equivalent diameter is proposed as the diameter of imaginary monodisperse-droplets which would bring about the same impingement rate as the polydisperse-droplets. The surface mean diameter $\bar{d}_{32}$, among mean diameters in common use, is found to be the closest to the proposed equivalent diameter.

Acknowledgements— The authors wish to express their gratitude to Professor M. Arie and Professor M. Kiya, Hokkaido University for their advice on an application of the inviscid bluff-body wake model, and to Research Associate M. Hongoh, Institute of High Speed Mechanics, Tohoku University for his assistance in drawing the figures.

REFERENCES

AIHARA, T., TAGA, M. & HARAGUCHI, T. 1979 Heat transfer from a uniform heat flux wedge in air–water mist flows. *Int. J. Heat Mass Transfer* **22**, 51–60.

AIHARA, T. & FU, W-S. 1982 Heat transfer from a wedge in air–water mist flow (theoretical study of a vertical infinite wedge of uniform wall temperature). *Trans. Japan Soc. Mech. Engrs. (Ser. B)* **48**, 2536–2546.

AIHARA, T., SHIMOYAMA, T., HONGOH, M. & FUJINAWA, K. 1985 Instrumentation and error sources for the measurement of the local drop-size distribution by an immersion-sampling cell. *Proceedings of 3rd International Conference on Liquid Atomisation and Spray Systems, London* **2**, VC/5/1–VC/5/11.

BRAGG, M. B. 1982 A similarity analysis of the droplet trajectory equation. *AIAA J.* **20**, 1681–1686.

GOLDSTEIN, M. E., YANG, W.-J. & Clark, J. A. 1967 Momentum and heat transfer in laminar flow of gas with liquid-droplet suspension over a circular cylinder. *Trans. ASME J. Heat Transfer* **89**, 185–194.

HODGSON, J. W. & SUNDERLAND, J. E. 1968 Heat transfer from a spray-cooled isothermal cylinder. *Ind. Eng. Chem. Fundam.* **7**, 567–572.

HEALY, J. V. 1970 Perturbed two-phase cylindrical type flows. *Phys. Fluids* **13**, 551–557.

HESS, J. L. 1973 Analytical solutions for potential flow over a class of semi-infinite two-dimensional bodies having circular-arc noses. *J. Fluid Mech.* **60**, 225–239.

HISHIDA, K., MAEDA, M. & IKAI, S. 1981 Study on heat transfer in a binary mist flow. *Trans. Japan Soc. Mech. Engrs. (Ser. B)* **47**, 1279–1286.

KIYA, M. & ARIE, M. 1977 An inviscid bluff-body wake model which includes the far-wake displacement effect. *J. Fluid Mech.* **81**, 593–607.

KUDO, K. & HIRATA, M. 1978 Sodium vapor deposition onto a horizontal flat plate above liquid sodium surface (concentration and diameter distributions of sodium mist in cover gas). *Trans. Japan Soc. Mech. Engrs.* **44**, 1025–1035.

LU, C. C. & HEYT J. W. 1980 Heat transfer from two-phase boundary layers on isothermal cylinder: Influence of drop trajectory. *AIChE J.* **26**, 762–768.

MORSI, S. A. & ALEXANDER, A. J. 1972 An investigation of particle trajectories in two-phase flow systems. *J. Fluid Mech.* **55**, 193–208.

NISHIKAWA, N. & TAKASE, H. 1979 Effects of particle-size and temparature difference on mist flow over a heated circular cylinder. *Trans. ASME J. Heat Transfer* **101**, 705–711.

THOMAS, W. C. & SUNDERLAND, J. E. 1970 Heat transfer between a plane surface and air containing suspended water droplets. *Ind. Eng. Chem. Fundam.* **9**, 368–374.

USHIKI, K., KUBO, K. & IINOYA K. 1977 Inertial separation of particle by ribbon (effects of incidence angle and deviation from Stokes drag). *Kagaku Kogaku Ronbunshu, Soc. Chem. Engrs. Japan.* **3**, 172–178.

APPENDIX A

Applicable range of the present numerical solutions

Strictly speaking, the present results and conclusions hold good only when all of assumptions (1)–(8) (see section 2) are satisfied; however, from a practical viewpoint their applicable range is examined further as follows.

Without ignoring the gravity, the equation of motion of a droplet in the x-direction should be expressed as:

$$\frac{\mathrm{d}U_d}{\mathrm{d}\tau} = \frac{C_D \mathrm{Re}_d}{24K} |\mathbf{W}_r| (U_G - U_d) + \frac{1}{Fr^2} , \qquad [28]$$

where Fr is the Froude number defined by

$$Fr = u_{G\infty} / \sqrt{gl} \qquad [29]$$

If we ignore the gravity, the collection efficiency η may be underestimated by 1–3% for the case of $Fr \simeq 7$. With further increases in Fr, the effect of gravity becomes negligible. In the case of much smaller values of Fr, although the gravity is not negligible, the effect of flow separation becomes negligible; therefore, existing results for a flow without separation is applicable. It should be incidentally added that assumption (6) produces an error less than 1% in the numerical results of $(Y_0)_{max}$ in the gravitational field.

As may be seen from [6] and [28], the governing variables of the droplet trajectories are K, Re_d and Fr alone; and Re_G has no direct effect on the present results, because the separation-bubble substantially keeps its shape near the body over the range of $\mathrm{Re}_G = 10^3$–10^5.

As is generally known, droplets remain nearly spherical at moderate values of Re_d if surface tension forces are strong; and the drag coefficient C_D for water drops in air is nearly equal to the standard drag curve for rigid spheres, for $\mathrm{Re}_d < 10^3$. Therefore, assumptions (4) and (5) hold good.

Furthermore it is also known that freestream turbulence up to 8% has a negligible effect on C_D for $\mathrm{Re}_d < 200$.

Consequently, it may be said that the present numerical results are applicable over the range of K and Re_d, more generally K_0 or $\overline{K}$, as shown in figure 2 and up to this turbulence intensity.

APPENDIX B

Mass flow rate of droplets entering the separated region

The mass flow rate $\dot{M}_f$ of droplets collected by the arc surface AB in figure 16 is given by

$$\dot{M}_f = \int_{(d_d)_{min}}^{(d_d)_{max}} G_{d\infty} (y_0)_{max} f_w \, \mathrm{d}d_d . \qquad [30]$$

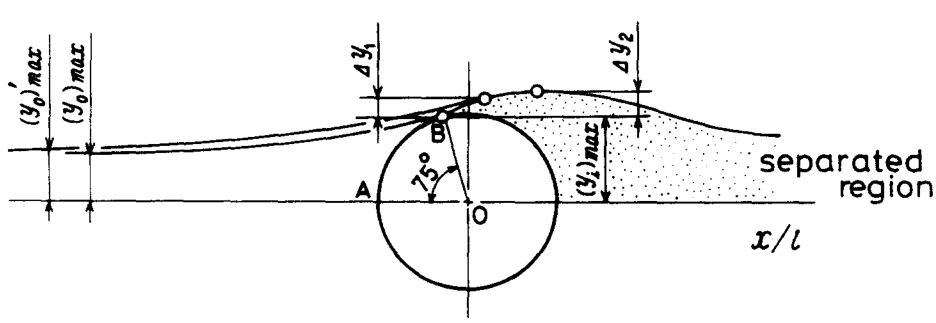

Figure 16. Droplets entering the separated region.

The mass flow rate $\dot{M}_s$ of droplets entering the separated region in the figure is expressed as

$$\dot{M}_s = \int_{(d_d)_{min}}^{(d_d)_{max}} G_{d\infty} \, \{(y_0)'_{max} - (y_0)_{max}\} \, f_w \, \mathrm{d}d_d \quad . \qquad [31]$$

Therefore, considering the relation $(y_0)'_{max} - (y_0)_{max} \leqq \Delta y_1 \leqq \Delta y_2$, we obtain

$$\frac{\dot{M}_s}{\dot{M}_f} \leqq \frac{\displaystyle\int_{(d_d)_{min}}^{(d_d)_{max}} \Delta y_2 \, f_w \, \mathrm{d}d_d}{\displaystyle\int_{(d_d)_{min}}^{(d_d)_{max}} (y_0)_{max} \, f_w \, \mathrm{d}d_d} \quad . \qquad [32]$$

The value of the right-hand side in the above equation is about 3% for a circular cylinder and 8% for a normal flat plate on an estimation for $n = 4$ and $d_c/l = 2 \times 10^{-3}$.